

Probably Unknown: Deep Inverse Sensor Modelling Radar

Rob Weston, Sarah Cen, Paul Newman and Ingmar Posner

Abstract—Radar presents a promising alternative to lidar and vision in autonomous vehicle applications, being able to detect objects at long range under a variety of weather conditions. However, distinguishing between occupied and free space from a raw radar scan is notoriously difficult. We consider the challenge of learning an Inverse Sensor Model (ISM) mapping a raw radar observation to occupancy probabilities in a discretised space. We frame this problem as a segmentation task, utilising a deep neural network that is able to learn an inherently probabilistic ISM from raw sensor data considers scene context. In doing so, our approach explicitly accounts for the heteroscedastic aleatoric uncertainty for radar that arises due to complex interactions between occlusion and sensor noise. Our network is trained using only partial occupancy labels generated from lidar and able to successfully distinguish between occupied and free space. We evaluate our approach on five hours of data recorded in a dynamic urban environment and show that it significantly outperforms classical constant false-alarm rate (CFAR) filtering approaches in light of challenging noise artefacts whilst identifying space that is inherently uncertain because of occlusion.

I. INTRODUCTION

Occupancy grid mapping has been extensively studied [1], [2] and successfully utilised for a range of tasks including localisation [3], [4] and path-planning [5]. One common approach to occupancy grid mapping uses an inverse sensor model (ISM) to predict the probability that each grid cell in the map is either *occupied* or *free* from sensor observations. Whilst lidar systems provide precise, fine-grained measurements, making them an obvious choice for grid mapping, they fail if the environment contains fog, rain, or dust [6]. Under these and other challenging conditions, radar is a promising alternative that is robust to changes in lighting and weather and detects long-range objects, making it well suited for use in autonomous transport applications.

However, occlusion and noise artefacts make distinguishing between occupied and free space in radar scans both difficult and uncertain. In contrast to a lidar ISM, this uncertainty is *heteroscedastic*, varying from one world location to another based on scene context, and *aleatoric* [7], in that it is inherent in radar data by way of the scan formation process. In order to successfully reason about world occupancy, we posit that a model that is able to reason about scene context is essential. To this end, we formulate the problem of determining an ISM as a segmentation task, leveraging a deep network. Our approach explicitly incorporates heteroscedastic aleatoric uncertainty, allowing us to learn the probability distribution of occupancy from raw data alone. We introduce a prior in regions of space where

Authors are from the Oxford Robotics Institute (ORI). This work was supported by training grant Programme Grant EP/M019918/1. We acknowledge use of Hartree Centre resources in this work. The STFC Hartree Centre is a research collaboratory in association with IBM providing High Performance Computing platforms funded by the UKs investment in e-Infrastructure. The Centre aims to develop and demonstrate next generation software, optimised to take advantage of the move towards exa-scale computing.

{robw, sarah, pnewman, ingmar}@robots.ox.ac.uk

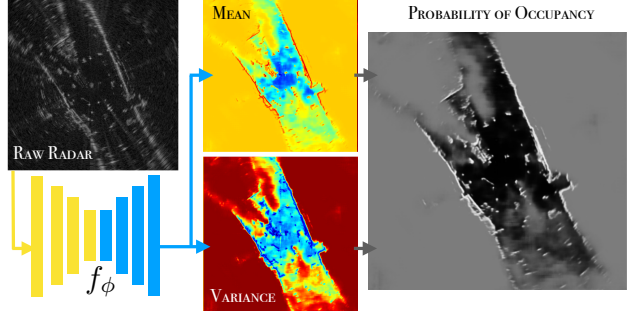


Fig. 1. Our network learns the distribution of occupancy from raw data and by reasoning about scene context, successfully identifies regions of space that are likely to be occupied and free in addition to determining what space is inherently unknown because of occlusion.

no training labels exist, allowing us to train our network with only partial observations generated from lidar data gathered at the same time as radar data and to learn from experience. At inference time, we efficiently and accurately determine the probability of occupancy through an analytic approximation, which avoids the need for sampling.

Our model is trained on real-world data generated from five hours of urban driving and successfully distinguishes between occupied and free space in light of challenging noise artefacts, outperforming constant false-alarm rate (CFAR) filtering whilst successfully identifying regions of space that are unknown due to occlusion. Our model is inherently probabilistic. We qualitatively show how this allows us to distinguish between uncertainty that can be captured through correlations between raw radar and the lidar labels and uncertainties that largely cannot. Finally, we show how fewer conservative priors on unlabelled space can be straightforwardly encoded into our loss.

II. RELATED WORK

Occupancy grids [1] are spatial representations that partition the environment into cells of equal size, and the state of each grid cell describes the probability that the associated region in space is occupied. Raw radar scans are often naively converted to binary occupancy grids using classical filtering techniques that distinguish between objects (or targets) and free space (or background). Common methods include CFAR [8] and static thresholding. However, both return binary labels rather than probabilities, and neither is capable of addressing all types of radar defects. Additionally, the most popular approach, CFAR, imposes strict assumptions on the noise distribution and requires manual parameter tuning.

Using lidar data, an ISM can be constructed using a combination of sensor-specific characteristics, experimental data, and empirically-determined parameters [9], [10], [11]. These human-constructed ISMs struggle to model radar defects that are not well understood and often utilise limited

local information to predict each cell's occupancy without accounting for scene context. For moving platforms, a world occupancy map can be sequentially generated from an ISM, multiple observations, and known robot poses using a binary Bayes filter [12]. In contrast, using deep learning methods, as first proposed by [13], allow for a more flexible ISM that better incorporates previous experiences and takes advantage of contextual information in the sensor observation.

In addition to *occupied* and *free*, an additional mutually exclusive *unknown state* can be introduced into occupancy grids using Dempster-Shafer decision theory [14]. Instead of this, we incorporate heteroscedastic aleatoric uncertainty into our formulation inspired by the work of [7]. Our variational re-formulation of [7] is closely related to the seminal works on variational inference in deep latent variable models [15], [16] and their extension to conditional distributions [17].

Drawing on the successes of deep segmentation in biomedical applications [18] and vision [19] we reformulate the problem of learning an inverse sensor model as neural network segmentation. Specifically, we utilise a U-net architecture with skip connections [20]. In order to map from an inherently polar sensor observation to a Cartesian map we utilise Polar Transformer Units (PTUs) [21].

III. DEEP INVERSE SENSOR MODELLING IN RADAR

A. Setting

Let $\mathbf{x} \in \mathbb{R}^{\Theta \times R}$ denote a full radar scan containing Θ azimuths of power returns at R different ranges for each full rotation of the sensor. Partitioning the world into a $H \times W$ grid, $\mathbf{y} \in \{0, 1\}^{H \times W}$ gives the occupancy state of each grid cell, where $\mathbf{y}^{u,v} = 1$ if cell (u, v) is *occupied* and $\mathbf{y}^{u,v} = 0$ if (u, v) is *free*. *Partial* measurements of occupancy $\hat{\mathbf{y}}$ are determined by combining the output of multiple 3D lidars and projecting the returns over a range of heights onto a 2D grid. In order to separate the region of space where no labels exist most likely as a consequence of full occlusion, from space that is likely to only be partially occluded or for which no labels exist due to a limited field of view of the lidar sensors, the observability state of each cell $\mathbf{o}^{u,v}$ is recorded as 0, 1 or 2 corresponding to *unobserved*, *observed* and *partially observed* space respectively. The full labelling procedure is described in Figure 2. This process is repeated for N radar-laser pairs to generate a data set $\mathcal{D} = \{\mathbf{x}^n, (\hat{\mathbf{y}}, \mathbf{o})^n\}_{n=1}^N$ of training examples from which we aim to learn an inverse sensor model $\mathbf{p}_{\mathbf{y}|\mathbf{x}} \in [0, 1]^{H \times W}$ such that $\mathbf{p}_{\mathbf{y}|\mathbf{x}}^{u,v} = p(\mathbf{y}^{u,v} = 1|\mathbf{x})$ gives the probability that cell (u, v) is occupied dependent on the *full* radar scan \mathbf{x} .

B. Heteroscedastic Aleatoric Uncertainty and FMCW Radar

FMCW Radar is an inherently noisy modality suffering from speckle noise, phase noise, amplifier saturation and ghost objects. These conspire to make the distinction between occupied and free space notoriously difficult. A radar's long range as well as its ability to penetrate past first returns make it attractive but also challenging. In particular, a radar's capacity for multiple returns along an azimuth implies

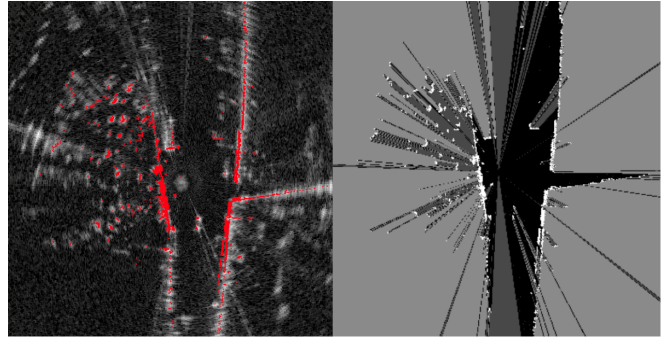


Fig. 2. Generated training labels from lidar. The image on the left shows the lidar points (red) projected into a radar scan \mathbf{x} converted to cartesian co-ordinates for visualisation. The right image shows the generated training labels. Any grid cell (u, v) with a lidar return is labelled as occupied $\hat{\mathbf{y}}^{u,v} = 1$ (white). Ray tracing along each azimuth, the space immediately in front of the first return is labelled as $\hat{\mathbf{y}}^{u,v} = 0$ (black). The space between the first and last return or along azimuths in which there is no return is labelled as *partially observed*, $\mathbf{o}^{u,v} = 2$, (dark grey) and the space behind the last return is labelled as *unobserved*, $\mathbf{o}^{u,v} = 0$, (light grey). Any space that is labelled as occupied or free is labelled as *observed*, $\mathbf{o}^{u,v} = 1$

varying degrees of uncertainty depending on scene context: the distinction between occupied and free space becomes increasingly uncertain as regions of space become partially occluded by objects. Examples of each of these problems are further explained in Figure 3. As such, high power returns do not always denote occupied and likewise, low power returns do not always denote free.

Uncertainties in our problem formulation depend on the world scene through a complex interaction between scene context and sensor noise, and are inherent in our data as a consequence of the image formation process. As such they are, heteroscedastic as they depend on scene context and aleatoric as they are ever present in our data [7]. In order to successfully determine world occupancy from an inherently uncertain radar scan we seek a model that explicitly captures heteroscedastic aleatoric uncertainty. By framing this problem as a deep segmentation task we leverage the power of neural networks to learn an ISM which accounts for scene context in order to determine – from raw data alone – *occupied* from *free* space in the presence of challenging noise artifacts.

C. Modelling Heteroscedastic Aleatoric Uncertainty

In order to incorporate heteroscedastic aleatoric uncertainty into our the model formulation, we treat the distance that the occupancy state of each cell $\mathbf{y}^{u,v}$ is predicted to fall away from the decision boundary as a normally distributed random variable $\mathbf{z}^{u,v}$ and model the mean $\boldsymbol{\mu}_\phi(\mathbf{x})$ and standard deviation $\boldsymbol{\gamma}_\phi(\mathbf{x})$ of \mathbf{z} using a neural network $f_\phi(\mathbf{x})$ [7] such that:

$$p_\phi(\mathbf{z}|\mathbf{x}) = \mathcal{N}(\mathbf{z}|\boldsymbol{\mu}_\phi(\mathbf{x}), \boldsymbol{\gamma}_\phi(\mathbf{x})\mathbf{I}) \quad (1)$$

$$[\boldsymbol{\mu}_\phi(\mathbf{x}), \boldsymbol{\gamma}_\phi(\mathbf{x})] := f_\phi(\mathbf{x}) \quad (2)$$

Assuming a likelihood $p(\mathbf{y}^{u,v} = 1|\mathbf{z}^{u,v}) = \text{Sigmoid}(\mathbf{z})$, the probability that cell $\mathbf{y}^{u,v}$ is occupied given radar scan \mathbf{x} is now given as,

$$p(\mathbf{y}^{u,v}|\mathbf{x}) = \int p(\mathbf{y}^{u,v}|\mathbf{z}^{u,v})p_\phi(\mathbf{z}^{u,v}|\mathbf{x})d\mathbf{z}^{u,v} \quad (3)$$

for which no exact closed form solution exists.

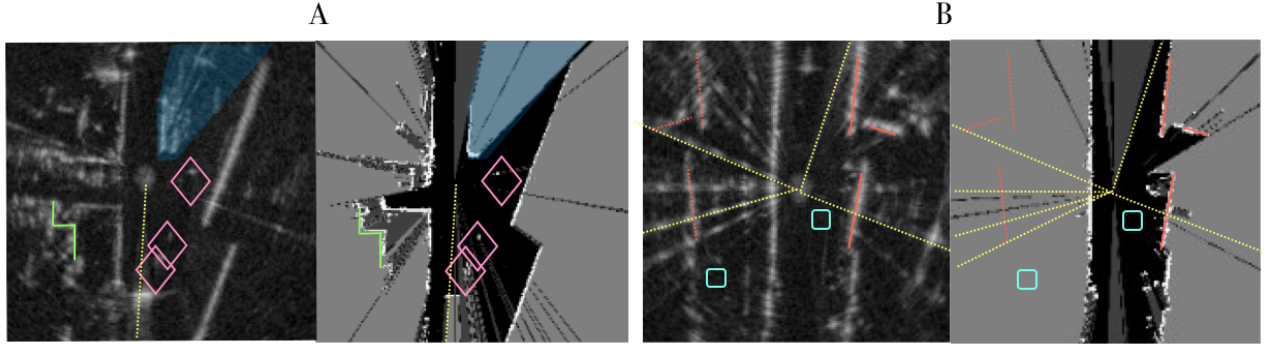


Fig. 3. Raw radar and the lidar ground truth. An ISM must be able to pick out faint objects, such as cars (pink diamonds), from the background speckle noise, in light of challenging noise artefacts such as saturation (yellow lines). In addition, an ISM must be able to determine what regions of space are likely to be occluded such as the space behind buses (highlighted blue) in light of almost identical local appearances (blue cyan boxes). Finally an ISM should be able to distinguish ghost objects (dotted orange) from true second returns (green lines).

Two problems present themselves in this formulation, (1) how do we train f_ϕ whilst explicitly encoding an assumption that in the absence of training labels we expect our model to be uncertain and (2) how do we accurately and efficiently calculate the posterior $p(\mathbf{y}^{u,v}|\mathbf{x})$? In Section III-D we introduce a normally distributed prior $p(\mathbf{z})$ on the region of space for which no training labels exist by utilising the variational inference framework. In Section III-E we consider an analytic approximation of (3) which accurately and efficiently predicts $p(\mathbf{y}^{u,v}|\mathbf{x})$ without resorting to sampling approaches.

D. Training with Partial Observations

In order to encode an assumption that in the absence of training data we expect our model to be explicitly uncertain we introduce to a prior $p(\mathbf{z}) = \mathcal{N}(\mathbf{z}|\boldsymbol{\mu}, \boldsymbol{\gamma}\mathbf{I})$ on the uncertainty associated with the region of space for which no training label exists, which our network reverts back to in the absence of a supervised training signal. To do this, we treat $p_\phi(\mathbf{z}|\mathbf{x})$ as an approximate posterior to $p(\mathbf{z}|\mathbf{y})$ induced by the joint $p(\mathbf{z}, \mathbf{y}) = p(\mathbf{y}|\mathbf{z})p(\mathbf{z})$ where,

$$p(\mathbf{y}|\mathbf{z}) := \prod_{u,v} \text{Bern}(\mathbf{y}^{u,v}|\mathbf{p}_{\mathbf{y}|\mathbf{z}}^{u,v}) \quad (4)$$

$$\mathbf{p}_{\mathbf{y}|\mathbf{z}}^{u,v} = p(\mathbf{y}^{u,v} = 1) = \text{Sigmoid}(\mathbf{z}^{u,v}) \quad (5)$$

$$p(\mathbf{z}) := \mathcal{N}(\mathbf{z}|\boldsymbol{\mu}, \boldsymbol{\gamma}\mathbf{I}) \quad (6)$$

Sigmoid and $\text{Bern}(y|p) = p^y(1-p)^{1-y}$ denote the element-wise sigmoid function and Bernoulli distribution. Given a set of observations \mathcal{D} , the parameters ϕ are therefore determined by maximising the variational lower bound,

$$\mathcal{L}(\phi; \mathcal{D}) = \sum_n \mathcal{L}^n(\phi) \quad (7)$$

$$\mathcal{L}^n(\phi) = \mathbb{E}_{p_\phi(\mathbf{z}|\mathbf{x}^n)}[\log p(\mathbf{y}^n|\mathbf{z})] - d_{kl}[p_\phi(\mathbf{z}|\mathbf{x}^n) \parallel p(\mathbf{z})] \quad (8)$$

The first term in $\mathcal{L}^n(\phi)$ is the expected log likelihood under the approximate posterior $p_\phi(\mathbf{z}|\mathbf{x})$ which when optimised forces the network to maximise the probability of each occupancy label \mathbf{y} . Crucially, the second term forces $p_\phi(\mathbf{z}|\mathbf{x})$ towards the prior $p(\mathbf{z})$, which allows us to encode assumptions on the uncertainty in cells for which no training label exists, regularising the output of our network in the absence of a supervised training signal. For a gaussian prior and approximate posterior the KL divergence term can be

determined analytically whilst the expected log-likelihood is estimated using the reparameterization trick [7] as,

$$\mathbb{E}_{p_\phi(\mathbf{z}|\mathbf{x})}[\log p(\mathbf{y}|\mathbf{z})] \approx -\frac{1}{L} \sum_l \left(\sum_{u,v} \mathbb{H}[\mathbf{y}^{u,v}, \mathbf{p}_{\mathbf{y}|\mathbf{z}}^{l,u,v}] \right) \quad (9)$$

where \mathbb{H} denotes binary cross entropy, $\mathbf{z}^l = \boldsymbol{\mu}_\phi(\mathbf{x}) + \boldsymbol{\gamma}_\phi(\mathbf{x}) \circ \boldsymbol{\epsilon}^l$ and $\boldsymbol{\epsilon}^l \sim \mathcal{N}(\mathbf{0}, \mathbf{I})$. We use our prior $p(\mathbf{z})$ to encode an assumption that in the absence of a training label we expect occupied and unoccupied space to occur with equal proportions by setting the mean $\boldsymbol{\mu} = \mathbf{0}$ and $\boldsymbol{\gamma} = \mathbf{I}$ in the unobserved region of space as judged by the lidar. In the observed and partially observed region of space the network is allowed to reason freely by setting the prior mean $\boldsymbol{\mu}$ and variance $\boldsymbol{\gamma}$ to the predicted mean $\boldsymbol{\mu}_\phi(\mathbf{x})$ and variance $\boldsymbol{\gamma}_\phi(\mathbf{x})$ respectively, setting the KL divergence term in (8) to zero in these regions.

As occupancy labels for unobserved and partially observed space are unavailable, the cross-entropy term is evaluated in the observed region only and to correct for this the expected model evidence is re-weighted by $\bar{\omega} = \omega HW / (\sum_{uv} \mathbb{I}(\mathbf{o}^{u,v} = 1))$. We include the hyper-parameter $\omega > 0$ to further weigh the relative importance between the likelihood and prior term. Finally, free space occurs with a significantly higher frequency and so we use weighted binary cross entropy $\mathbb{H}_{\bar{\alpha}}$ [22],

$$\mathbb{H}_{\bar{\alpha}}[y, p] = \frac{n_- + n_+}{(1 + \bar{\alpha})n_-} \left(\bar{\alpha}y \log(p) + (1 - y) \log(1 - p) \right) \quad (10)$$

where $\bar{\alpha} = \alpha \frac{n_-}{n_+}$, n_+ and n_- are the number of positive and negative labels in $\hat{\mathbf{y}}$, and α is a hyper-parameter used to weigh the relative importance of occupied versus free space.

Our final loss function becomes:

$$\begin{aligned} \hat{\mathcal{L}}^n(\phi) = & \bar{\omega} \sum_{l,u,v} \mathbb{I}(\mathbf{o}^{u,v} = 1) \mathbb{H}_{\bar{\alpha}}[\hat{\mathbf{y}}^{n,u,v}, \mathbf{p}_{\mathbf{y}|\mathbf{z}}^{n,l,u,v}] \\ & + d_{kl}[p_\phi(\mathbf{z}|\mathbf{x}^n) \parallel p(\mathbf{z})] \end{aligned} \quad (11)$$

$$\hat{\mathcal{L}}(\phi; \mathcal{D}) = \frac{1}{N} \sum_n \hat{\mathcal{L}}^n(\phi) \quad (12)$$

There is no loss in the *partially observed* region, allowing the network to freely reason from the model evidence in observed space and the KL divergence in unobserved space, allowing model training with only partial laser observations.

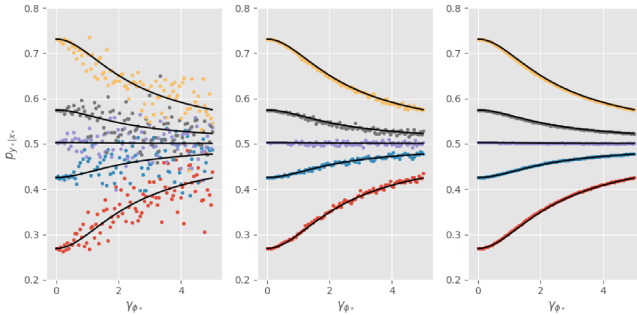


Fig. 4. Predicted occupancy probabilities $p_{y|x}$ as a function of predicted standard deviation $\gamma_{\phi*}$ using the analytic approximation given by (17) (black) vs Monte Carlo approximation with $L = 10^2$ (left), $L = 10^4$ (middle) and $L = 10^6$ (right) samples. Each colour corresponds to a different mean $\mu_{\phi*}$ with [yellow, grey, purple, blue, red] corresponding to means $[-1, -0.3, 0.01, 0.3, 1]$ respectively. It is seen that the MC estimate has high variance taking of the order 10^6 samples to converge to the analytic approximation. On the other hand the analytic approximation closely resembles the converged Monte Carlo estimate.

E. Inference

Given a trained model $p_{\phi*}(z|x) = \mathcal{N}(z|\mu_{\phi*}(x), \gamma_{\phi*}(x))$ we now wish to determine the probability that each cell is occupied given input x marginalising out the uncertainty associated with the latent variable z :

$$p(y^{u,v}|x) := \int p(y^{u,v}|z^{u,v})p_{\phi*}(z^{u,v}|x)dz^{u,v} \quad (13)$$

However, for likelihood $p(y^{u,v}|z^{u,v}) = \text{Sigmoid}(z^{u,v})$ no exact closed form solution exists to this integral. Instead of resorting to Monte Carlo sampling we approximate the sigmoid function with a probit function and use the result that a gaussian distribution convolved with a probit function is another probit function [23]. Following this analysis, it can be shown that,

$$p(y^{u,v} = 1|x) \approx \text{Sigmoid}\left(\frac{\mu_{\phi*}^{u,v}}{s_{\phi*}^{u,v}}\right) \quad (14)$$

where $s_{\phi*}^{u,v} = (1 + (\gamma_{\phi*}^{u,v} \sqrt{\pi/8})^2)^{1/2}$, $\mu_{\phi*}^{u,v} = \mu_{\phi*}(x_*)$ and $\gamma_{\phi*}^{u,v} = \gamma_{\phi*}^{u,v}(x_*)$. This allows us to efficiently calculate $p_{y|x}$ as,

$$[\mu_{\phi*}, \gamma_{\phi*}] = f_{\phi*}(x) \quad (15)$$

$$s_{\phi*} = (1 + (\gamma_{\phi*} \sqrt{\pi/8})^2)^{1/2} \quad (16)$$

$$p_{y|x} := \text{Sigmoid}\left(\frac{\mu_{\phi*}}{s_{\phi*}}\right) \quad (17)$$

Figure 4 shows $p_{y|x}$ approximated using (17) and Monte Carlo sampling for varying $\mu_{\phi*}$ and $\gamma_{\phi*}$. The Monte Carlo estimate takes of the order 10^4 samples to converge, whilst the analytic approximation provides a close approximation to the converged Monte Carlo estimate. In addition to predicting the probability of occupancy of each cell $p_{y|x}$ our model allows us to quantify the decision and aleatoric uncertainty associated with the new radar scan x through $\mu_{\phi*}$ and $\gamma_{\phi*}$ respectively.

By incorporating heteroscedastic aleatoric uncertainty into our formulation, there are now two mechanisms by which our model can express uncertainty, as can be seen from (17). The predicted mean $\mu_{\phi*}$ gives the distance an example is *expected* to fall from the decision boundary. The greater the magnitude of $|\mu_{\phi*}|$, the lower the entropy of

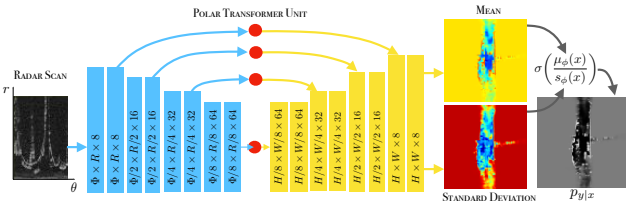


Fig. 5. Our network architecture takes in a polar radar scan $x \in \mathbb{R}^{\Theta \times R}$ and maps it to Cartesian grids of mean utility μ_{ϕ} and aleatoric noise scale $s_{\phi} = (1 + (\gamma_{\phi} \sqrt{\pi/8})^2)^{1/2}$. Our network is composed of a polar (blue) encoder and a Cartesian (yellow) decoder. At each polar to Cartesian interface there is a polar transformer unit (red circle). Each blue rectangle corresponds to 2 convolutions followed by a max pool.

the predicted distribution. On the other hand $\gamma_{\phi*}$ gives the predicted standard deviation in the prediction, and acts like the temperature parameter of a Boltzmann distribution, increasing the entropy of the distribution of occupancy $p_{y|x}$ independent of how far an example is predicted to fall away from the decision boundary. The uncertainties communicated by each parameter are investigated in Section IV-C. The mean $\mu_{\phi*}$ captures uncertainties that can easily be explained through correlations between our raw radar input and training label, whilst the predicted standard deviation $\gamma_{\phi*}$ captures uncertainty that arises through random events independent of the true class of each world location, such as occlusion.

IV. RESULTS

We show that our model, despite challenging noise artefacts, is able to successfully segment the world into occupied and free space achieving higher mean Intersection over Union (IoU) scores than CFAR filtering approaches, whilst in addition correctly identifying regions of space that are unknown due to occlusion. We provide a qualitative study of the uncertainties expressed through the mean $\mu_{\phi}(x)$ and the standard deviation $\gamma_{\phi}(x)$ predicted by our network showing that the predicted mean largely captures uncertainties that can be determined from correlations between our radar data and the training labels whilst the predicted standard deviation captures uncertainties that largely cannot. By using scene context our network is able to intelligently reason and distinguish between different uncertainties in each of these cases. We show that by changing the relative weighting between the expected model evidence and KL divergence terms in (11), we can encode less conservative priors on the region of space for which no training labels exist. Finally, we provide several qualitative examples of the occupancy grids generated in a range of challenging real-world scenes.

A. Experimental Set-Up

A Navtech CTS350x radar and two Velodyne HDL32 Lidars were mounted to a survey vehicle and used to generate over 78000 (90%) training examples and 8000 (10%) test examples from urban scenes. The output from the two lidars was combined from 0.7m below the roof of the vehicle to 1m above and projected onto a 600×600 grid, with a spatial resolution of 0.3m, generating a $180m \times 180m$ world occupancy map, following the procedure described in Section III-A. Figure 5 shows our network architecture

in which a polar encoder takes the raw radar output and generates a polar feature tensor through repeated applications of 4×4 convolutions and max pooling before a Cartesian decoder maps this feature tensor to a grid of means $\mu_\phi(\mathbf{x}) \in \mathbb{R}^{H \times W}$ and standard deviations $\gamma_\phi(\mathbf{x}) \in \mathbb{R}^{H \times W}$ which are converted to a grid of probabilities through (17). Information is allowed to flow from the encoder to the decoder through skip connections, where polar features \mathbf{u} are converted to Cartesian features \mathbf{v} through bi-linear interpolation, with a fixed polar to Cartesian grid [21]. In all experiments we trained our model using the ADAM optimiser [24], with a learning rate of 0.001, batch size 16 for 100 epochs and randomly rotated each input output pair about the origin, minimising the loss proposed in (11) with $L = 25$ samples. Experimentally it was found that setting $\alpha = 0.5$ gave the best results in terms of IoU performance against the lidar labels. Unless otherwise stated, the model evidence importance was set to $\omega = 1$.

B. Detection Performance of Deep ISM vs Classical Filtering Methods

We compare the detection performance of our approach against CFAR [8] applied in 1D (along range) for polar scans and in 2D for Cartesian scans by determining the quantity of occupied and unoccupied space successfully segmented in comparison to the ground truth labels generated from lidar in observed space. Due to class frequency imbalance, we use the mean Intersection Over Union (IoU) metric [25]. The optimum number of guard cells, grid cells and probability of false alarm, for each CFAR method, was determined through a grid search maximising the mean IoU of each approach on training data. For our method, each cell was judged as occupied or free based on a 0.5 probability threshold on $p_{y|x}$. A 2m square in the centre of the occupancy map, corresponding to the location of the survey vehicle, was marked as unobserved.

The results from the test data set for each approach are shown in table I and show that our approach outperforms all the tested CFAR methods, increasing the performance in occupied space by 0.11, whilst achieving almost the same performance in free space leading to a mean IoU of 0.63. Our model is successfully able to reason about occupied space in light of challenging noise artefacts. In contrast, the challenge in free space is not in identification, with free space typically being characterised by low power returns, but in distinguishing between observed and unobserved regions, a challenge which is missed entirely by the IoU metric. Figure 6a shows how our model is able to successfully determine space that is likely to be unknown because of occlusion and is able to clearly distinguish features, such as cars that are largely missed in CFAR.

C. Uncertainty Prediction

As described in Section III-E, by incorporating aleatoric uncertainty into our formulation, our network is able to express uncertainty through the mean $\mu_\phi(\mathbf{x})$ and the predicted variance $\gamma_\phi(\mathbf{x})$. In order to show which uncertainties are captured by each of these mechanisms, we segment the world

TABLE I
COMPARING OUR APPROACH TO CLASSICAL DETECTION METHODS
USING INTERSECTION OVER UNION

Method	Intersection over Union		
	Occupied	Free	Mean
CFAR (1D polar)	0.24	0.92	0.5
CFAR (2D Cartesian)	0.20	0.90	0.55
Static thresholding	0.19	0.77	0.48
Deep ISM (our approach)	0.35	0.91	0.63

into occupied, free and unknown space by thresholding the absolute distance each cell is predicted to fall away from the decision boundary $|\mu_\phi(\mathbf{x})|$ and the standard deviation associated with that prediction $\gamma_\phi(\mathbf{x})$ respectively. The results of this process for decreasing confidence thresholds are shown in Figure 6d. The predicted mean distance from the decision boundary successfully captures uncertainties that can be explained through correlations between our raw radar input and the training labels. For example, walls in radar manifest as a peak of power returns in front of and behind their labelled location in lidar, a relationship that is consistent throughout the data set and is captured, through $\mu_\phi(\mathbf{x})$, by positioning space in front of and behind the labelled wall location closer to the decision boundary.

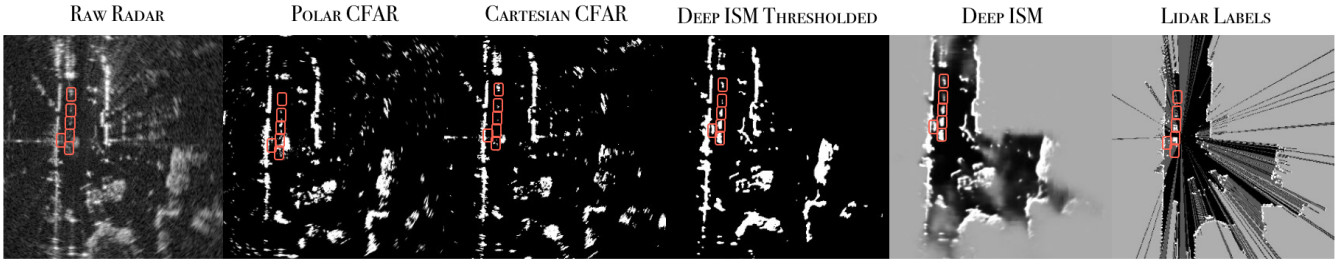
The standard deviation predicted by our network largely captures uncertainty caused by occlusion, which, independent of the true underlying state of occupancy, results in space that is inherently unknown. From least likely to most likely to be occluded, we move from high power returns labelled as occupied, to a region nearby and up to the first return, to space that lies in partial and full occlusion. This ray tracing mechanism is largely captured by the standard deviation $\gamma_\phi(\mathbf{x})$ predicted by our network.

D. Qualitative Results

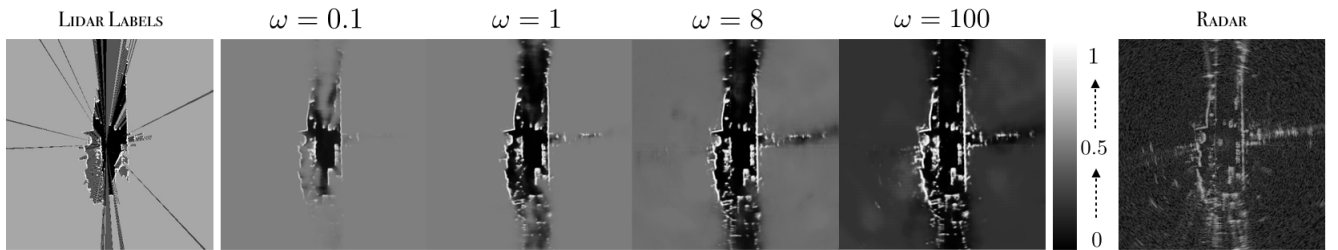
In Figure 6b we vary the relative importance between the likelihood and KL divergence term by varying the hyper-parameter ω in (11). Increasing ω increases the relative importance of the likelihood term and leads to an ISM which is able to more freely reason about regions of space for which no labels exist during training, using the labels available in the observed scene. This allows a practitioner to encode, more or less conservative priors based on there specific use case. Finally, Figure 6c gives a qualitative examples taken from the test set. Our network is able to successfully reason about the complex relationship between observed and unobserved space in light of challenging noise artefacts.

V. CONCLUSION

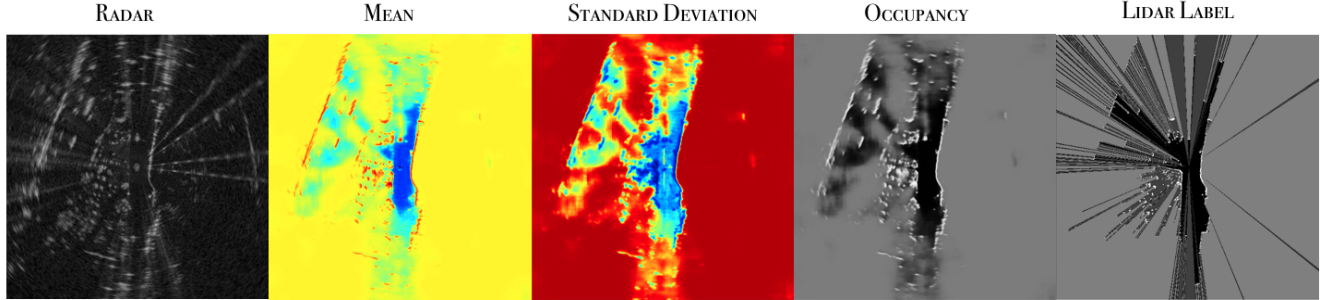
By using a deep network we are able to learn – from raw data alone – an inherently probabilistic ISM which, by accounting for scene context, can successfully identify regions of space that are likely to be occupied or free, in light of challenging noise artefacts, whilst simultaneously identify regions of space that are inherently unknown due to occlusion. At present, our approach does not take account of temporal consistency between frames which we posit should further improve the learnt probability distribution of occupancy. We leave this for future work.



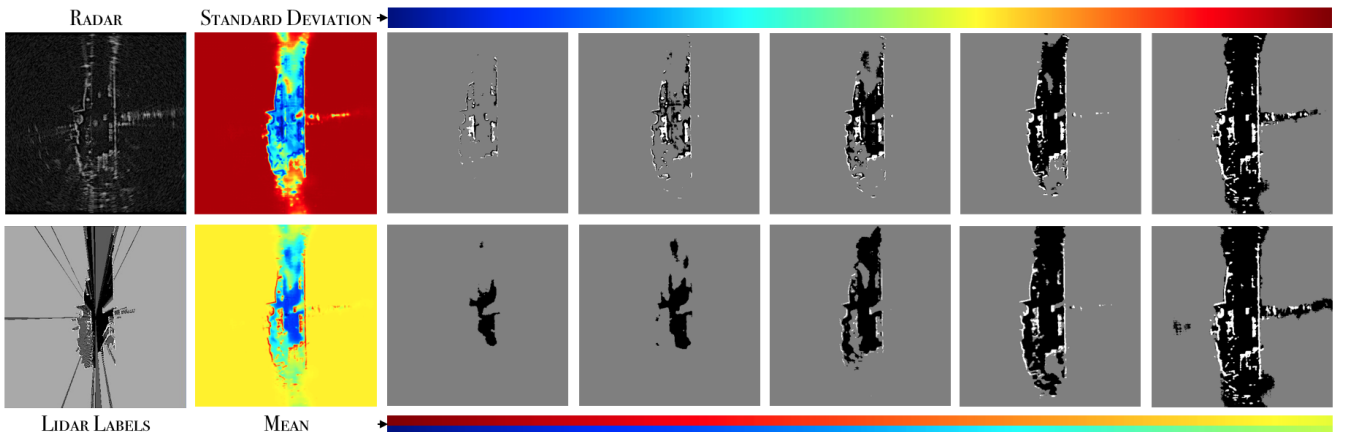
(a) The detection performance of our approach vs classical filtering methods with black representing predicted free and white representing predicted occupied by each approach. In comparison to CFAR our approach results in crisp and clean detections in observed and unobserved space. The red rectangles highlight cars that are clearly detected by our approach which are largely missed by CFAR. In addition, our model is able to successfully reason about what in the scene is likely to be unknown due to occlusion.



(b) The predicted probability of occupancy for different values of likelihood importance ω . As ω is increased our model becomes increasingly less conservative, reasoning in the unobserved region of space based on labels in the observed region.



(c) Our model successfully identifies occupied and occluded space in challenging real world environments.



(d) A scene segmented as predicted occupied (white), unoccupied (black) and unknown (grey) for decreasing confidence thresholds (left to right) on the predicted standard deviation γ_ϕ (top) and mean μ_ϕ (bottom). The standard deviation is generally low in regions of high power returns for which there is consistent correlation between the raw radar power returns and the lidar that can largely be captured by the mean. In almost all cases in which labels exist, low power returns correspond to free space, however, low power returns also arise in occlusion. In light of this, free space is positioned far from the decision boundary (bottom), but with a relatively high standard deviation (top).

REFERENCES

- [1] A. Elfes, "Using occupancy grids for mobile robot perception and navigation," *Computer*, no. 6, pp. 46–57, 1989.
- [2] K. Konolige, "Improved occupancy grids for map building," *Autonomous Robots*, vol. 4, no. 4, pp. 351–367, 1997.
- [3] A. Milstein, "Occupancy grid maps for localization and mapping," in *Motion Planning*, InTech, 2008.
- [4] D. Filliat and J.-A. Meyer, "Map-based navigation in mobile robots:: I. a review of localization strategies," *Cognitive Systems Research*, vol. 4, no. 4, pp. 243–282, 2003.
- [5] J.-A. Meyer and D. Filliat, "Map-based navigation in mobile robots:: II. a review of map-learning and path-planning strategies," *Cognitive Systems Research*, vol. 4, no. 4, pp. 283–317, 2003.
- [6] B. Clarke, S. Worrall, G. Brooker, and E. Nebot, "Towards mapping of dynamic environments with fmew radar," in *Intelligent Vehicles Symposium Workshops (IV Workshops), 2013 IEEE*, pp. 140–145, IEEE, 2013.
- [7] A. Kendall and Y. Gal, "What uncertainties do we need in bayesian deep learning for computer vision?", in *Advances in Neural Information Processing Systems*, pp. 5580–5590, 2017.
- [8] M. Skolnik, *Radar Handbook, Third Edition*. Electronics electrical engineering, McGraw-Hill Education, 2008.
- [9] K. Werber, M. Rapp, J. Klappstein, M. Hahn, J. Dickmann, K. Dietmayer, and C. Waldschmidt, "Automotive radar gridmap representations," in *Microwaves for Intelligent Mobility (ICMIM), 2015 IEEE MTT-S International Conference on*, pp. 1–4, IEEE, 2015.
- [10] R. Dia, J. Mottin, T. Rakotovao, D. Puschini, and S. Lescop, "Evaluation of occupancy grid resolution through a novel approach for inverse sensor modeling," *IFAC-PapersOnLine*, vol. 50, no. 1, pp. 13841–13847, 2017.
- [11] S. Thrun, "Learning occupancy grid maps with forward sensor models," *Autonomous robots*, vol. 15, no. 2, pp. 111–127, 2003.
- [12] M. Adams, M. D. Adams, and E. Jose, *Robotic navigation and mapping with radar*. Artech House, 2012.
- [13] S. B. Thrun, "Exploration and model building in mobile robot domains," in *Neural Networks, 1993., IEEE International Conference on*, pp. 175–180, IEEE, 1993.
- [14] D. Pagac, E. M. Nebot, and H. Durrant-Whyte, "An evidential approach to map-building for autonomous vehicles," *IEEE Transactions on Robotics and Automation*, vol. 14, no. 4, pp. 623–629, 1998.
- [15] D. J. Rezende, S. Mohamed, and D. Wierstra, "Stochastic backpropagation and approximate inference in deep generative models," *arXiv preprint arXiv:1401.4082*, 2014.
- [16] D. P. Kingma and M. Welling, "Auto-encoding variational bayes," *arXiv preprint arXiv:1312.6114*, 2013.
- [17] K. Sohn, H. Lee, and X. Yan, "Learning structured output representation using deep conditional generative models," in *Advances in Neural Information Processing Systems*, pp. 3483–3491, 2015.
- [18] H. R. Roth, C. Shen, H. Oda, M. Oda, Y. Hayashi, K. Misawa, and K. Mori, "Deep learning and its application to medical image segmentation," *Medical Imaging Technology*, vol. 36, no. 2, pp. 63–71, 2018.
- [19] X. Liu, Z. Deng, and Y. Yang, "Recent progress in semantic image segmentation," *Artificial Intelligence Review*, pp. 1–18, 2018.
- [20] O. Ronneberger, P. Fischer, and T. Brox, "U-net: Convolutional networks for biomedical image segmentation," in *International Conference on Medical image computing and computer-assisted intervention*, pp. 234–241, Springer, 2015.
- [21] C. Esteves, C. Allen-Blanchette, X. Zhou, and K. Daniilidis, "Polar transformer networks," *arXiv preprint arXiv:1709.01889*, 2017.
- [22] J. Long, E. Shelhamer, and T. Darrell, "Fully convolutional networks for semantic segmentation," in *Proceedings of the IEEE conference on computer vision and pattern recognition*, pp. 3431–3440, 2015.
- [23] N. M. Nasrabadi, "Pattern recognition and machine learning," *Journal of electronic imaging*, vol. 16, no. 4, p. 049901, 2007.
- [24] D. P. Kingma and J. Ba, "Adam: A method for stochastic optimization," *arXiv preprint arXiv:1412.6980*, 2014.
- [25] M. Everingham, L. Van Gool, C. K. Williams, J. Winn, and A. Zisserman, "The pascal visual object classes (voc) challenge," *International journal of computer vision*, vol. 88, no. 2, pp. 303–338, 2010.